Small Target Detection Based on Noncoherent Radial Velocity Spectrum of High-Resolution Sea Clutter

Sai-Nan Shi , Peng-Lang Shui , *Senior Member, IEEE*, Xiang Liang , and Tao Li

Abstract—This article proposes a multiscan joint noncoherent detection method of small targets in high-resolution sea clutter with spatial–temporally structural textures induced by large-scale swells and waves, which is composed of intrascan noncoherent integration at each spatial resolution cell followed by interscan integration on a radial velocity template. The main contributions of the article are as follows. First, a concept of noncoherent radial velocity spectrum (NCRVS) is proposed to model the nonhomogeneity of multiscan integration of sea clutter with structural textures. In the NCRVS, the noncoherent intrascan integration and the interscan integration by passing the retrospective filter bank are fully combined. Second, the NCRVS of sea clutter has different statistics at individual radial velocity bins and the lognormal distributions are used to fit their statistics and an outlier-robust analytical bipercentile estimator is constructed for parameter estimation. Third, based on the lognormal-distributed NCRVS model, a double-channel multiscan joint detector (DC-MJD) is proposed, where the intrascan noncoherent integration channel is used to find floating or low radial velocity targets and the whitening plus intrascan noncoherent integration channel is used to find target with high radial velocity. Simulated data and measured X-band radar data are used to verify the DC-MJD detector. In comparison with the existing three multiscan detectors, the DC-MJD detector improves the detection probability by 96% in the measured data with a test target.

Index Terms—Bipercentile estimator, multiscan joint detection, noncoherent radial velocity spectrum (NCRVS) of sea clutter, sea clutter, small target detection.

I. INTRODUCTION

ONE of the main tasks of high-resolution fast-scan maritime surveillance radars is to find sea-surface small targets, such as small boats, frogmen, periscopes [1], [2], [3], [4]. This is a difficult task because of the intra- and interscan complicated characteristics of high-resolution sea clutter and low signal-to-clutter ratios (SCR) of target radar returns. It is a key precondition to model sea clutter in a long-time interval across intrascan and interscan.

In a short time scale of tens of milliseconds, the compound Gaussian models (CGM) with various distributed textures have been developed to model sea clutter [5], [6], which forms the foundation of intrascan coherent/noncoherent target detection in sea clutter. Under the CGM, sea clutter is represented as the product of a slow-varying texture from the power modulation by swells and large-scale wind waves and fast-varying complex Gaussian speckle from the backscattering of small-scale wind waves and capillary waves whose wavelengths are comparable with the operating wavelength of the radar. Probability density functions (PDF) to model textures include the biparametric Gamma distributions [5], inverse Gamma distributions [7], inverse Gaussian distributions [8], lognormal distributions [9], and triparametric distributions [10], [11]. These distributions can meet statistical modeling of textures in sea clutter at different spatial resolution and sea states but fail to reflect texture temporal correlation along pulses and spatial correlation along range and azimuth. As the radar resolution gets higher, spatial–temporally characteristics of sea clutter are modulated by swells and large-scale waves and often exhibit approximately periodic behavior in a time scale of the order of seconds [12], [13]. Modeling sea clutter across time scales is necessary for high-resolution fast-scan maritime radars to improve mall target detection.

High-resolution fast-scan maritime radars often detect small targets by the intrascan coherent/noncoherent integration of radar returns at individual spatial resolution cells followed by interscan binary/amplitude integration along a radial velocity template [14], [15], [16]. Small target detection in sea clutter relies on either sufficient radial velocity difference of targets relative to the Doppler offset of sea clutter or discernible interscan paths of targets relative to sea spikes. For sea-surface small targets of low radial velocities, such as periscopes of submarines, intra- and interscan joint detection must be used because of their low observable radar returns. The intrascan noncoherent log-cell-averaging constant false alarm rate (CFAR) detection and interscan binary integration using a retrospective filter bank (RFB) on the range-scan time grids form an effective scheme, which has been verified by the antisubmarine radars [15]. The fan-shaped templates of retrospective filters achieve a perfect compromise between line integration and robustness to translation compensation error of the radar platform and target maneuvering. For joint detection scheme using intrascan coherent detection, the scan rate and dwelling time are two key factors to affect performance. From the high-resolution X-band

data with small boats under test, it is revealed that faster scan rates with shorter dwelling time provide an improved detection performance over slower scan rates with longer dwelling time [16]. Moreover, at high-resolution and small grazing angle, it is found that the main factors to affect detection of slow-moving small targets are spatially sparse sea spikes of high intensity and the internal noise of radar receiver. In the ε-contaminated mixture Gaussian model of sparse sea spikes plus Gaussian noise, the noncoherent slow target adaptive detector on the pulse-range grids is developed [17], which is a typical "image-to-detect" method and exhibits quite robust and good detectability in measured data of the APS-137 radar for antisubmarine [15]. The fast scan-to-scan integration processing (FSSIP) detector consists of the intrascan amplitude integration followed by the interscan CFAR on the range-scan time grids, which exhibits fair detectability in Gaussian noise or homogeneous sea clutter [18]. In [19], the intrascan optimum coherent integration under the generalized Pareto distribution of sea clutter and the multiple feature integration via Doppler guided retrospective filters are combined to form a multiscan joint detection scheme and it first exploits the inconsistency between the Doppler offset of sea clutter in intrascan coherent processing interval of tens of milliseconds and the interscan radial movement of swells and large-scale waves. It attains obvious improvement in detection of slow-moving small targets in high-resolution sea clutter with structural textures.

The common foundation of all the multiscan joint detection is modeling sea clutter across time scales from radar slow time to scan time. This article first proposes the concept of the non-coherent radial velocity spectrum (NCRVS) of high-resolution sea clutter. It reflects the across-scale statistical characteristics of high-resolution sea clutter when the intrascan processing uses noncoherent or whitened noncoherent integration and the interscan uses RFB-based integration. At each radial velocity bin, the mean of the NCRVS of sea clutter is its power and the NCRVS at different radial velocities exhibits different statistics except power. It is found that the NCRVS has the maximal variance when the radial velocity equals to the radial velocity of swells and large-scale waves on the sea surface. From the analysis of real measured data, the lognormal distributions are used to model the NCRVS of sea clutter at individual radial velocity bins. In this way, the NCRVS of sea clutter is modeled by a set of biparametric lognormal distributions at individual radial velocity bins that share a scale parameter and have different shape parameters. Under the lognormal-distributed NCRVS model, a double-channel multiscan joint detection (DC-MJD) method is presented. The first channel is designed to find small targets whose Doppler offsets fall outside the main clutter region of sea clutter and the intrascan whitened noncoherent integration is used. The second channel is designed to find small targets whose Doppler offsets fall into the main clutter region and the intrascan noncoherent integration is used, like the zero-velocity filter in the traditional MTD signal processor [35]. At last, the binary results of the two channels are fused by the "or" logical operator. The proposed detection scheme is verified by real measured X-band high-resolution radar data and is compared with other multiscan joint detection methods.

This article is organized as follows. Section II reviews the operating mode and signal model of high-resolution fast-scan maritime radars and the general framework of multiscan joint detection. Section III introduces the concept of the NCRVS of sea clutter, proposes lognormal distribution modeling of the NCRVS of sea clutter, and gives outlier-robust bipercentile estimator of the model parameters. In the lognormal-distributed NCRVS model, a DC-MJD scheme is proposed. Section IV demonstrates experimental results on real measured radar data and compared the proposed detection scheme with other multi-scan joint detection schemes. Finally, we conclude our article in Section V.

II. REVIEW OF SIGNAL MODEL AND MULTISCAN JOINT DETECTION FRAMEWORK OF HIGH-RESOLUTION FAST-SCAN MARITIME RADAR

A. Signal Model for Multiscan Joint Detection

High-resolution maritime surveillance radars often operate at two modes to find sea-surface small targets: fast-scan and short dwelling time mode and long dwelling time mode [16]. The first mode attains more scan-to-scan integration of target returns and less coherent pulse-to-pulse integration. Differently, the second mode encounters inhomogeneous sea clutter and nonparametric target returns models due to long dwelling time and target detection is made by sophisticated feature-based detection [36], [37], [38] instead of simple intra- and interscan integration. Here, we focus on the fast-scan mode where the scan rate is over 60 rpm and the dwelling time at each beam position is within 10 ms.

At the fast-scan mode, radar returns on one azimuth beam form a 3D data of range, pulse, and scan time. The pulse dimension is at a short time scale of the order of milliseconds and there are often a few pulses at a scan for noncoherent or coherent integration. The scan time is in a time scale of the order of seconds and there are often tens of scans for integration. High-resolution radars often use an appropriate range resolution such that sea-surface small targets of interest are point-like targets occupying a range cell. Target detection on one azimuth beam uses radar data at multiple contiguous range cells and multiple consecutive scans. The multiscan joint detection boils down to the following binary hypothesis test problem [18], [19]

$$\begin{cases} H_0 : z(m, n, k) = c(m, n, k) \\ H_1 : z(m, n, k) = s(m, n, k) + c(m, n, k) \end{cases} \quad (1)$$
$$m = 1, 2, \cdots ; n = 1, \ldots, N; k = 1, \ldots, K$$

where $z(m, n, k)$ is radar returns of the nth pulse and kth scan at the mth range cell, $s(m, n, k)$ denotes target returns, $c(m, n, k)$ is sea clutter, N is the number of pulses at one scan, and K is the number of scans. The multiscan joint detection is to decide whether there exists a target on a special range-scan cell (m, n, k) from the K scans of radar returns. In other words, it needs to retrospect the first $(K-1)$ scan of radar data to decide whether there exists one target at one range cell at the present scan [the Kth scan in (1)].
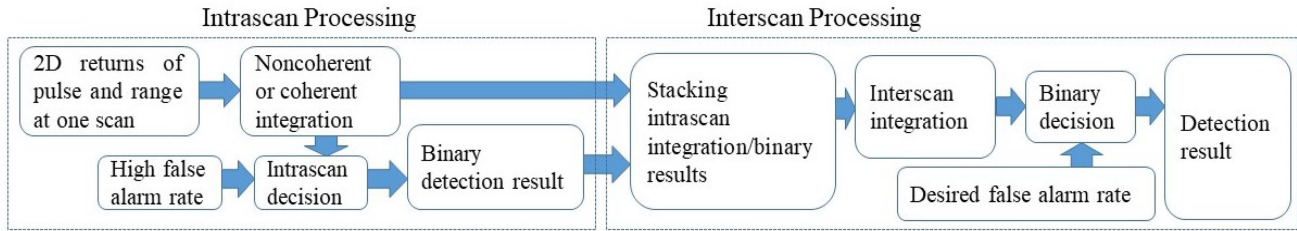
Fig. 1. Basic framework of multiscan joint detection in high-resolution fast-scan maritime radars.

B. Multiscan Joint Detection Framework at Fast-Scan Mode

For maritime radars operated at fast-scan mode, the basic framework of small target detection contains intrascan and interscan processing to integrate target returns and mitigate sea clutter and noise. The intrascan processing includes coherent or noncoherent integration and integration gain of target returns is limited by the number of pulses available at one scan. Not high integration of the intrascan processing is not enough to realize effective detection of small targets and effective exclusion of sea spike alarms. In a short time scale of tens of milliseconds for intrascan integration, sporadic sea spikes of high intensity are likely to be misjudged as targets because sea spikes last from a few tenths of a second to several seconds [20], [21]. The interscan amplitude/power or binary integration in a time scale of the order of seconds can improve target detection and exclude false alarms from sea clutter and sea spikes [22]. Fig. 1 illustrates a basic framework of multiscan joint detection in high-resolution fast-scan maritime radars to detect small targets. The intrascan processing transfers the multiple pulse data at a scan into test statistics or binary result by coherent/noncoherent integration and detection. The intrascan processing results at multiple successive scans are stacked into a 2-D real-valued or binary image along range cells and scan time. Different types of interscan integration methods are used to implement an effective integration along possible path of a small target. The interscan processing excludes false alarms from sea clutter and sea spikes.

Existing multiscan joint detection methods can be interpreted as a realization of the basic framework in Fig. 1. In [15], noncoherent Log-CFAR detector and the peak-pick threshold are combined into the intrascan processing to yield a primary binary decision result at a high false alarm rate. And then, the interscan binary integration using the RFB is used for final decision. In [19], the generalized likelihood ratio test with linear threshold detector (GLRT-LTD), which is the optimum coherent detector in compound-Gaussian sea clutter with the inverse Gamma-distributed textures [40], is used as the intrascan processing to generate the plot data, their test statistic and Doppler offsets. Stacking these data on the range-scan time plane in the interscan processing, the three features are extracted by the integration using the Doppler-guided retrospective filter (RF) for final decision. It exploits the inconsistency between the Doppler offset of sea clutter in the time scale of the order of milliseconds and the movement of the structural textures of sea clutter in the time scale of the order of seconds and thus markedly reduces false alarms from structural textures of sea clutter. The FSSIP

detector in [18] uses the intrascan noncoherent integration and interscan path integration using line search and works well in homogeneous environments with few sea spikes.

It can be seen that existing multiscan joint detection schemes are all involved in the cross-scale integration of sea clutter from radar slow time to scan time. However, the model of sea clutter is restricted in the scale of radar slow time and does not match the cross-scale integration in multiscan joint target detection. The work in [19] mentioned the inconsistency between the Doppler offset of sea clutter in the scale of radar slow time and the movement of structural texture of sea clutter in the scale of radar scan time but does not go deep into cross-scale modeling of sea clutter. It is important to develop cross-scale sea clutter model from radar slow time to scan time for multiscan joint target detection in fast-scan maritime radars.

III. MULTISCAN JOINT DETECTION UNDER LOGNORMAL-DISTRIBUTED NCRVS MODEL OF SEA CLUTTER

A. Cross-Scale NCRVS Model of Sea Clutter

It is well-known that sea clutter can be modeled by the product of a slowly-varying random variable (texture component) and a fast-varying multivariate complex Gaussian random vector (speckle component) [5], [6]. Speckle results from the short wind wave and capillary wave scatterings and it shows the intrascan Doppler velocity of sea clutter in a short time scale of the order of milliseconds [29], [30]. Differently, texture is generated from tilt modulation of swells or large-scale waves [8], [11]. When the range resolution is smaller than the wavelength of swells, sea clutter appears the spatial–temporally structural textures in a time scale of the order of seconds. Because the long waves propagate faster than the short swells and capillary waves, Doppler velocity of sea clutter is less than the radial moving velocity of swells to generate the structural textures. It is meaning that the velocities of sea clutter in different scales show different properties. In fact, the macroscopical structural textures of sea clutter reflect the time-evolving intensity variances of rough sea surface. To describe the complicated electromagnetic scattering coefficients of rough sea surface, many semiempirical models for sea-surface backscattering coefficients are developed, such as SIT model, GIT model, and TSC model [27], [28]. Those models are established on the empirical expressions, determined by radar parameters of radar wave length, polarization mode, grazing angle of radar, and sea environment parameters of wind height, wind speed, sea state. However, the statistical properties of the spatial–temporally intensity of sea clutter are absent in
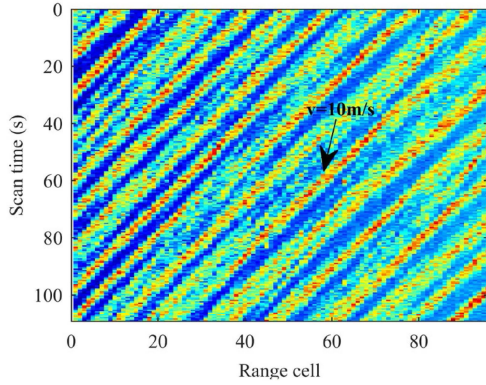
Fig. 2.   Real sea clutter data in range-scan time grids.

Fig. 3.   Flowchart of two kinds of cross-scale NCRVS model.

the current article. Therefore, a cross-scale NCRVS is proposed to describe the properties of sea clutter in a time scale of tens of milliseconds and in a time scale of the order of seconds.

Fig. 2 plots 2-D intensity map of real CSIR dataset (TFC15_002) [31] on the range-scan time grids, with the range resolution of 15 m and the pulse repetition frequency (PRF) of 2500 Hz. The dwelling dataset is transferred to scan data with a scan period of $\Delta T = 0.5\,\text{s}$ and pulse number of $N = 8$. In the range-scan time 2-D plane, spatial–temporally structural textures present zebra stripes alternating bright and dark strips. The bright stripes generated from the title scattering reflect the moving trajectories of swells and large-scale waves, aggravating the clutter's heavy tail in PDF. The dark strips of low intensities are from the backscattering of trough of waves. The radial velocity of sea clutter in a time scale of the order of seconds is about 10 m/s, while the radial Doppler velocity of sea clutter is 2.9 m/s and the Doppler bandwidth is about 300 Hz in a time scale of tens of milliseconds. It is noted that the resolution of Doppler spectrum is low due to the few pulses at one scan. In the high resolution of Doppler spectrum using hundreds of pulses, the radial Doppler velocity of sea clutter is 1.5 m/s and the Doppler bandwidth is about 200 Hz.

In the NCRVS model, intrascan processing and interscan processing are combined to build a bridge across different time scales for the first time. Fig. 3 gives the flowchart of the two kinds of NCRVS models, including the whitening operator, intrascan noncoherent integration, RFB, and multiscan integration. The first kind of NCRVS has the intrascan noncoherent integration, designed for the low-velocity target detection. The second kind of NCRVS has the whitening operator plus the intrascan noncoherent integration, designed for the high-velocity target detection. These two models are independent for two cases.

In the intrascan processing, due to several pulses available for integration at fast-scan mode, the intrascan integration is generally limited. In order to mitigate the sea clutter, whitening operator is given in the second kind of NCRVS, where pulse correlation of sea clutter is eliminated and clutter spectrum is uniformly distributed in the frequency domain. In CGM, sea clutter vector $\mathbf{c} = [c(1), c(2), \ldots, c(N)]^{\text{T}}$ is modeled by [5], [6]
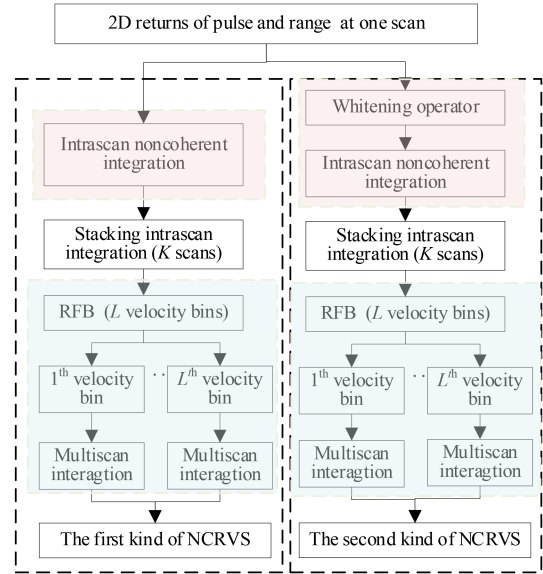
$$\mathbf{c} = \sqrt{\tau}\,\mathbf{u} \tag{2}$$

where τ is texture component and $\mathbf{u}$ is speckle component of the speckle covariance matrix $\mathbf{M} = \text{E}(\mathbf{u}\mathbf{u}^{\text{H}})$. Then, whitening operator is defined by

$$\tilde{\mathbf{c}} = \mathbf{M}^{-1/2}\mathbf{c} \tag{3}$$

where $\tilde{\mathbf{c}}$ is the whitened observation vector. In this way, sea clutter is preprocessed to obtain the unit speckle covariance matrix $\text{E}(\tilde{\mathbf{c}}\tilde{\mathbf{c}}^{H}) = \tau\mathbf{I}_N$, independent of the pulse correlation.

In the real environment, the speckle covariance matrix is unknown and its estimation can be computed by the normalized sample covariance matrix [26] from the reference cells. Assumed that the number of reference range cells is P and their return vectors are denoted by $\mathbf{c}_p, p = 1, 2, \ldots, P$. It is given by

$$\widehat{\mathbf{M}} = \frac{N}{P}\sum_{p=1}^{P}\frac{\mathbf{c}_p\mathbf{c}_p^{\text{H}}}{\mathbf{c}_p^{\text{H}}\mathbf{c}_p}. \tag{4}$$

Substituting the (4) into (3), it achieves the whitened operator. Moreover, whitening operator can improve the SCR when Doppler offset of target falls outside the main clutter region in Doppler domain.

As for the intrascan noncoherent integration, short-time intensity integration is used. It is computed by

$$I\left(m,k\right) = \begin{cases} \frac{1}{N}\sum_{n=1}^{N}\left|c(m,n,k)\right|^2, & \text{first kind of NCRVS} \\ \frac{1}{N}\left|\widehat{\mathbf{M}}^{-1/2}\mathbf{c}(m,k)\right|^2, & \text{second kind of NCRVS} \end{cases} \tag{5}$$

where $\mathbf{c}(m, k)$ is the clutter vector at the mth range cell and the kth scan.

In the interscan processing, the current scan and the previous $(K-1)$ scans are combined for multiscan integration. In the time scale of the order of seconds, the radial velocities of interesting low-velocity small targets are assumed to be constant during a few seconds. Typically, the local Hough-transform search [30] can accumulate the dispersed intensity of targets along
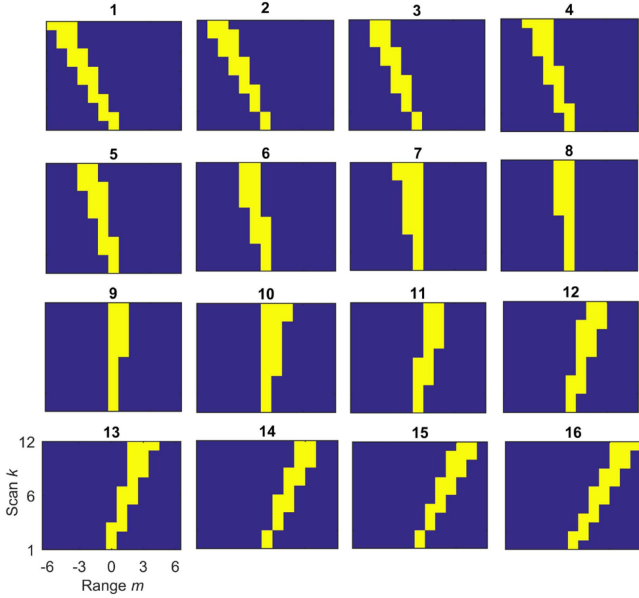
Fig. 4. Example of RFB design ($K = 12$ and $L = 16$).

straight-line moving trajectories. However, due to the translation compensation error of the radar platform, velocities of targets often fluctuate in a small range during the several seconds, causing the nonlinear line of target's moving trajectories.

Assume that the center velocity is v m/s and the variation interval of velocity is $\Delta \nu$. The fan-shaped template of the RF is designed by

$$\text{RF}_{\nu, \Delta \nu}(m, k) =$$
$$\begin{cases} 1, & fix\left(\frac{k(v-0.5\Delta v)\Delta T}{\Delta r}\right) \leq m \leq fix\left(\frac{k(v+0.5\Delta v)\Delta T}{\Delta r}\right) \\ 0, & \text{otherwise} \end{cases}$$
$$(6)$$

where ΔT is scan period of the radar and Δr is the range resolution. Then, a bank of retrospective filters is well-designed to fully cover the speed range of interesting targets, realizing the conversion from time series to different velocity bins. When the radial velocity interval of interesting targets is given as $[-v_{\max}, v_{\max}]$, the center velocities of the L retrospective filters are uniformly sampled according the radial velocity interval

$$v_l = -v_{\max} + \frac{2v_{\max}}{L} \times (l - 0.5), l = 1, 2, \ldots, L. \quad (7)$$

The variation interval of velocity $\Delta \nu$ meets the requirement

$$\Delta v_l \geq \frac{2v_{\max}}{L}. \quad (8)$$

It can ensure the adjacent filters to be partly overlapped.

Fig. 4 plots an example of RFB design when $K = 12, L = 16$, $\Delta T = 0.5$ s, $\Delta r = 15$ m, and $v_{\max} = 15$ m/s. At each velocity bin, fan-shaped trajectory starts from the current scan to $(L-1)$ history scans, which is determined by the center speed v_l and velocity interval $\Delta \nu$ in (7). In this way, multiscan integration only occurs along the well-designed moving trajectory and sea clutter with inconsistent speed can be completely suppressed. Thus,

RFB has the significant selective properties of radial velocity in the range-scan time grids, which is similar to the role of Fourier transform in Doppler domain. Besides, each RF has fan-shaped trajectory to solve the translation compensation error of the radar platform. Therefore, RFs can distinguish the sea clutter from the perspective of velocity property in a time scale of the order of seconds.

Thus, NCRVS is established by passing the well-designed RFB in (6) and (7). It is defined by

$$\text{NCRVS}(m \,|v_l\,) = I(m, k) \otimes_{RF} \text{RF}_{v_l, \Delta v}(m, k)$$
$$= \frac{1}{K} \sum_{k=1}^{K} \max_{m:\text{RF}_{v_l, \Delta v}(m,k)=1} \{I(m, k)\},$$
$$l = 1, 2, \ldots, L \quad (9)$$

where $\otimes_{RF}$ denotes the nonlinear integration via RF. For sea clutter, Doppler spectrum exhibits the microcosmic velocity property in a short time scale of the order of milliseconds. While NCRVS reveals the macroscopic velocity property in a time scale of the order of seconds, which can be recognized as a new domain.

Below, we investigate the properties of NCRVS at individual velocity bins. For convenience, the second kind of NCRVS is discussed as example in the following parts. Fig. 5 shows the second kind of NCRVS distributions of sea clutter at three typically RFs with center velocities of -15, -1, and 9 m/s. It is clearly found that NCRVS is nonuniformly distributed at each individual velocity bin. At the first RF, there exists small gap of NCRVS values from range cells located in the bright stripes and in the dark strips, and integration is partly mitigated due to the inconsistent velocity between center velocity of RF and the radial velocity of swells and large-scale waves. In the eighth RF, the integration along the bright strips becomes great, since the center velocity of RF is close to the movement velocity of swells. When the two velocities fully match at the 14th RF, integration sharply fluctuates when range cells are located in the bright strips and in the dark strips. This phenomenon is determined by the structural textures of sea clutter in the range-scan time 2-D plane, showing the cross-scale statistical characteristics of spatial–temporally sea clutter in a new way.

B. Lognormal-Distributed NCRVS Model and Bipercentile Estimation

In order to describe quantitatively the multiscan integration fluctuation, we discuss the statistical properties at individual velocity bins. Due to the dynamic sea environments, NCRVS of sea clutter is assumed to be a random process. Then, two numerical characters of mean $\mu_{N,K}$ and standard deviation $\sigma_{N,K}$ are given to further characterize the statistical property.

Generally, the mean and standard deviation of NCRVS are unknown in the real detection environments and it should be estimated from the large amount of sea clutter. At the lth RF,
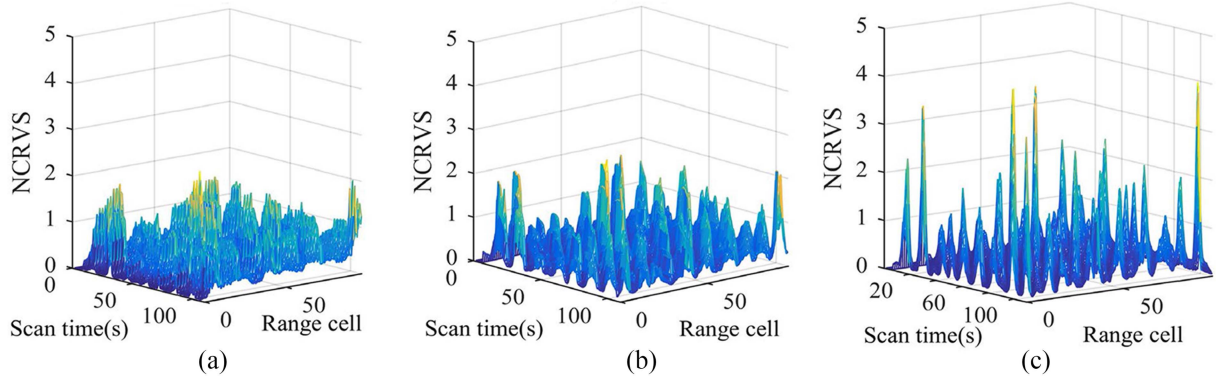
Fig. 5.   NCRVS distributions at three typical velocity bins (the second kind). (a) 1th RF of v = −14m/s. (b) 8th RF of v = −1m/s. (c) 14th RF of v = 10m/s.
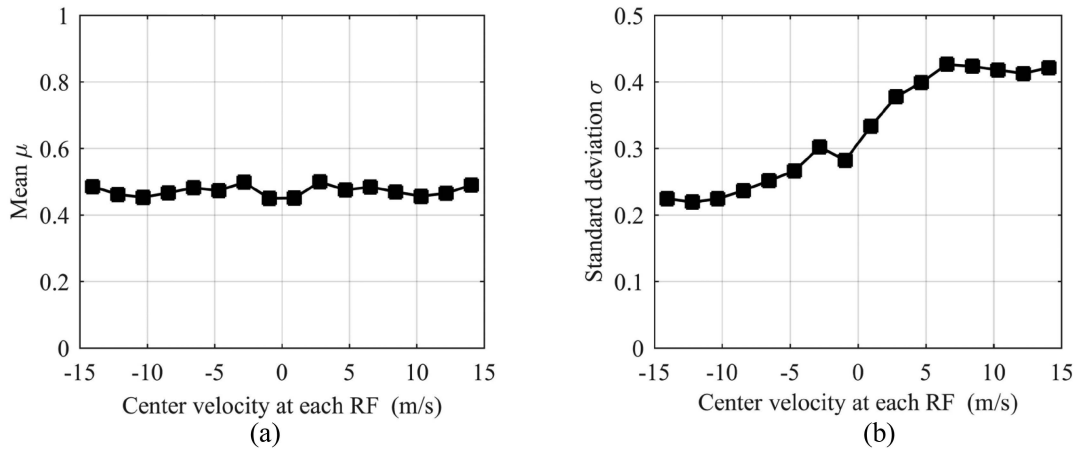

Fig. 6.   Numerical characters of NCRVS at each velocity bin (the second kind). (a) Mean function. (b) Standard deviation function.

they can be computed by

$$\hat{\mu}_{N,K}(v_l) = \frac{1}{M} \sum_{m=1}^{M} \text{NCRVS}(m \,|v_l)$$

$$\hat{\sigma}_{N,K}(v_l) = \sqrt{\frac{1}{M-1} \sum_{m=1}^{M} \left(\text{NCRVS}(m \,|v_l) - \hat{\mu}_{N,K}(v_l)\right)^2}$$

$$\tag{10}$$

where M is the number of sea clutter range cells that can be collected in quantity from the current clutter environment once marine radar is turned ON.

In Fig. 6(a), mean functions maintain constant at different velocity bins, reflecting the average intensity of sea clutter in the pulse-range-scan time 3-D grids. In Fig. 6(b), standard deviation is computed independently at each velocity bin. The large values of standard deviation imply sharp fluctuation of NCRVS, which generates from the integration gap along bright strips and dark strips. It means that the center velocity of RF with maximum standard deviation matches the radial moving velocity of swells to generate the structural textures. Considering the dispersion of swell width and the overlapped velocity in RF design, the

average center velocity of 9.37 m/s from adjacent 12th to 15th RFs provides a rough estimation of radial moving velocity of swells and large-scale waves. As the center velocity after 15th RF is far away from the real radial velocity of 10 m/s, the standard deviation is bound to go down.

In fact, it is difficult to theoretically derive the PDF of NCRVS model at individual velocity bins, due to the nonlinear operations and complicated processing to generate the NCRVS of sea clutter. In terms of the great fluctuation at the main clutter RFs, lognormal distribution with heavy tail is presented to fit the NCRVS at individual velocity bins, further elaborating the NCRVS in statistic. The PDF of lognormal distribution is defined by

$$p_{\text{LN}}(x) = \frac{1}{x\lambda\sqrt{2\pi}} \exp\left(-\frac{(\text{In}(x) - \eta)^2}{2\lambda^2}\right), x > 0 \tag{11}$$

where λ is the shape parameter, η is scale parameter, and $\text{In}(x)$ follows the Gaussian distribution with mean η and standard deviation λ, i.e, $\text{In}(x) \sim N(\eta, \lambda)$.

Considering the existence of outliers in the real complicated clutter environments, a bipercentile estimation method with robustness to outliers is proposed to estimate the two unknown
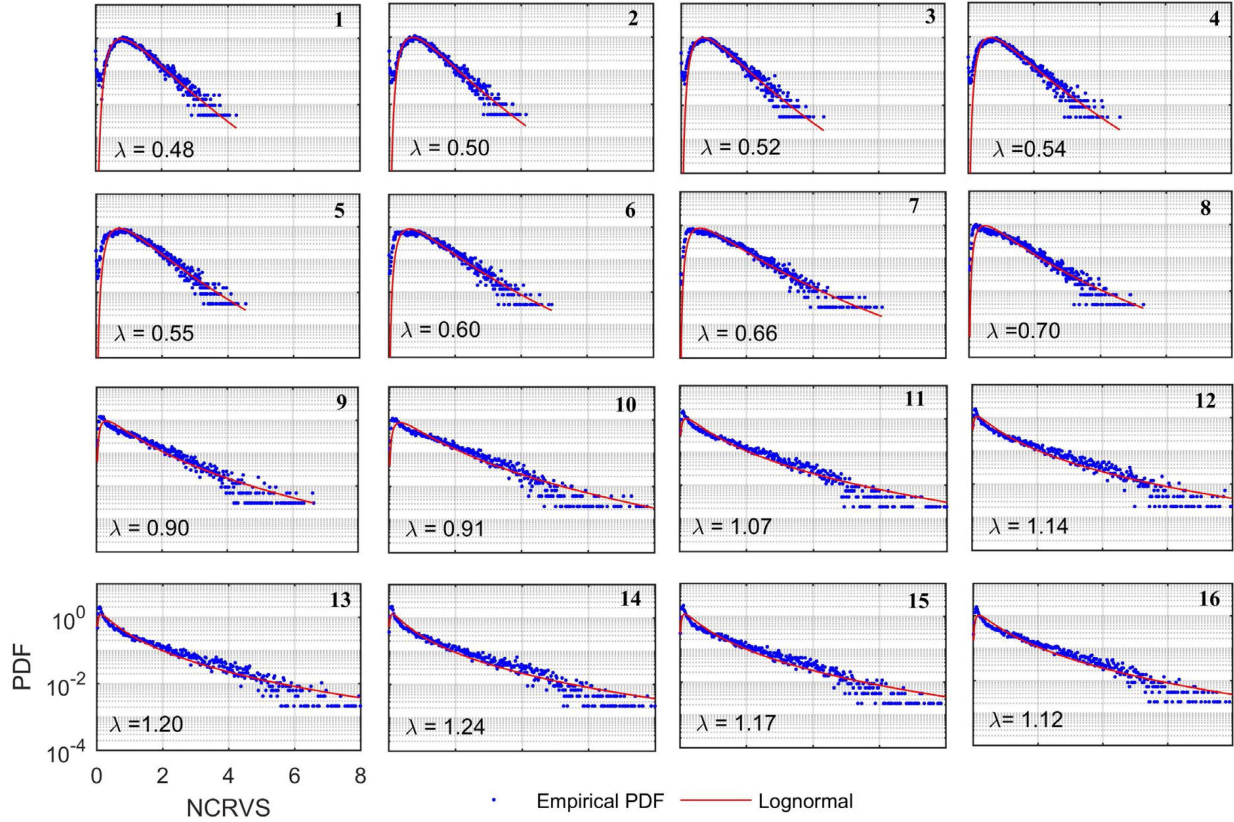
Fig. 7. First kind NCRVS fitting by lognormal distributions at each velocity bin.

parameters in (11). The cumulative distribution function of lognormal distribution is given by

$$F_x(x) = \frac{1}{2} + \frac{1}{\sqrt{\pi}} \int_0^{\frac{\ln(x)-\eta}{\sqrt{2}\lambda}} e^{-y^2} dy = \frac{1}{2} + \frac{1}{2}\text{erf}\left(\frac{\ln(x)-\eta}{\sqrt{2}\lambda}\right) \tag{12}$$

where $\text{erf}(\cdot)$ is error function that is monotone increasing in the positive domain at a given two percentiles α_1 and α_2. Then, it obtains the following two expressions:

$$\begin{cases} F_x(x_1) = \frac{1}{2} + \frac{1}{2}\text{erf}\left(\frac{\ln(x_1)-\eta}{\sqrt{2}\lambda}\right) = \alpha_1 \\ F_x(x_2) = \frac{1}{2} + \frac{1}{2}\text{erf}\left(\frac{\ln(x_2)-\eta}{\sqrt{2}\lambda}\right) = \alpha_2. \end{cases} \tag{13}$$

In this way, the two unknown parameters can be computed by

$$\begin{cases} \eta = \frac{\beta\ln(x_2)-\ln(x_1)}{\beta-1}, \quad \beta = \frac{\text{erf}^{-1}(2\alpha_1-1)}{\text{erf}^{-1}(2\alpha_2-1)} \\ \lambda = \frac{\ln(x_2)-\eta}{\sqrt{2}\text{erf}^{-1}(2\alpha_2-1)}. \end{cases} \tag{14}$$

For the M samples at each velocity bin, sort from the smallest to the largest according to their values, denoted as $s_1 \le s_2 \le, \ldots, \le s_M$. Then, the estimation values of x_1, x_2 are

$$\widehat{x_1} = s_{[M \times \alpha_1]}, \quad \widehat{x_2} = s_{[M \times \alpha_2]} \tag{15}$$

where [] is round number operator. In the theory, any two percentiles can be used to estimate the shape and scale parameters in the lognormal distribution.

For convenience, set the two percentiles $\alpha_1 = 0.5$ and $\alpha_2 = 0.9$. According to the table values of error function, the values of inverse function are given by $\text{erf}^{-1}(0) = 0$, $\text{erf}^{-1}(0.8) = 0.9062$. Thus, the equations in (14) can be simplified by

$$\widehat{\eta} = \ln(\widehat{x_1}); \widehat{\lambda} = \frac{\ln(\widehat{x_2}) - \widehat{\eta}}{\sqrt{2}\text{erf}^{-1}(0.8)}. \tag{16}$$

This bipercentile estimation method has analytical expressions and can resist the abnormal values to maintain the robust estimation even in the complicated environments.

In the experiments, six distributions of Rayleigh, Gamma, Weibull, K, inverse Gaussian, and lognormal are tested and the results show the best good fit of lognormal distribution. For clear, Figs. 7 and 8 plot the fitting results by the lognormal distributions at individual velocity bins for the two kinds of NCRVS, where the number in the top right corner is corresponding to the number of RF and the shape parameters are plotted in the left bottom. It is found that the NCRVS at each velocity bin is well fitted by the lognormal distribution, as the average value of Kolmogorov–Smirnov test are 0.0686 and 0.0261 at the two kinds of NCRVS. The two kinds of NCRVS have the same statistical properties, only different in the shape parameter and scale parameter at each velocity bin. Additionally, the main clutter RFs have obvious greater shape parameters than others RFs, meaning that structural textures have great influence on detection. Shape parameters can offer statistical properties of structural textures of sea clutter in another way. Therefore, the
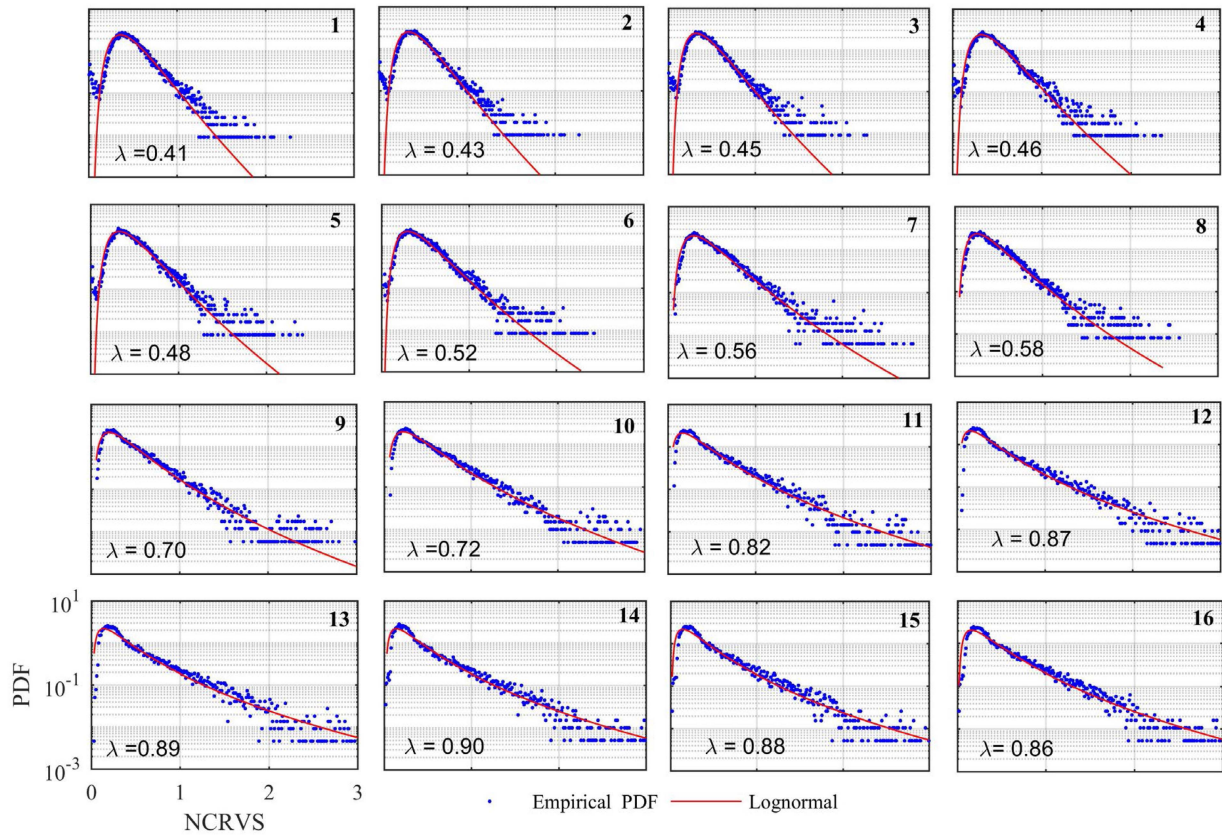
Fig. 8. Second kind NCRVS fitting by lognormal distributions at each velocity bin.

first and the second moments of NCRVS at each velocity bin can be served as the main statistical properties.

For the Doppler spectrum in a time scale of the order of milliseconds, sea clutter is nonuniformly distributed in the Doppler bins, where the Doppler bins with the maximum values are recognized as the main clutter bins and that of smaller values are called noise bins. Like Doppler spectrum, NCRVS is nonuniformly dispersed at individual velocity bins. RFs with great fluctuation integration or large shape parameters of lognormal distributions are referred to as the main clutter RFs, such as the 12th to 15th RFs in Figs. 6–8. While RFs with small fluctuation integration or small shape parameters of lognormal distribution are regarded as the noise RFs, the remaining RFs whose center velocities are inconsistent with the radial velocity of swells and large-scale waves. In this way, it is easier for marine radars to detect small targets in the noise RFs than that in the main clutter RFs, since the multiscan integration of sea clutter in the main clutter RFs are likely to be great. Therefore, it is important to mitigate the clutter integration in the main clutter RFs and improve the low SCR of small targets for the following detection.

C. Double-Channel Multiscan Joint Detector

In the lognormal-distributed NCRVS model, sea clutter has different statistical properties with nonuniformly dispersion of standard deviation. The main clutter RFs may lead to many false alarm range cells located in the structural textures of bright

strips. To guarantee the desired false alarm rate, traditional detectors have to elevate the decision threshold, resulting in the low detection probability. Thus, it is required to mitigate sea clutter at each velocity bins, especially the clutter in the main clutter RFs.

In order to suppress sea clutter, different threshold is set at each velocity bin, which is determined by the false alarm rate, shape parameter and scale parameter in lognormal distribution. Besides, two kinds of NCRV are combined to form two channels for detection of small targets. Fig. 9 gives the detection flow diagram of DC-MJD. In the first channel, radar returns use the noncoherent integration to attain short-time pulse gain in the intrascan processing. Then, it is separately processed at each velocity bin, followed by the multiscan integration to establish the first kind of NCRVS. The real value of NCRVS is compared with decision threshold at each velocity bin and all the binary results from L velocity bins are fused by the "or" logical operator. In the second channel, whitening operator at one scan is added and the others are the same as the first channel. Finally, binary results from the two channels are again fused by the "or" logical operator.

In fact, whitening operator mainly aims to delimitate the pulse correlation of sea clutter and balance the nonuniform spectrum in the intrascan processing. The whitening spectrum can make the great influence on the SCR of small targets. When the Doppler offsets of targets fall outside the main clutter region in the frequency domain, whitening operator can attain
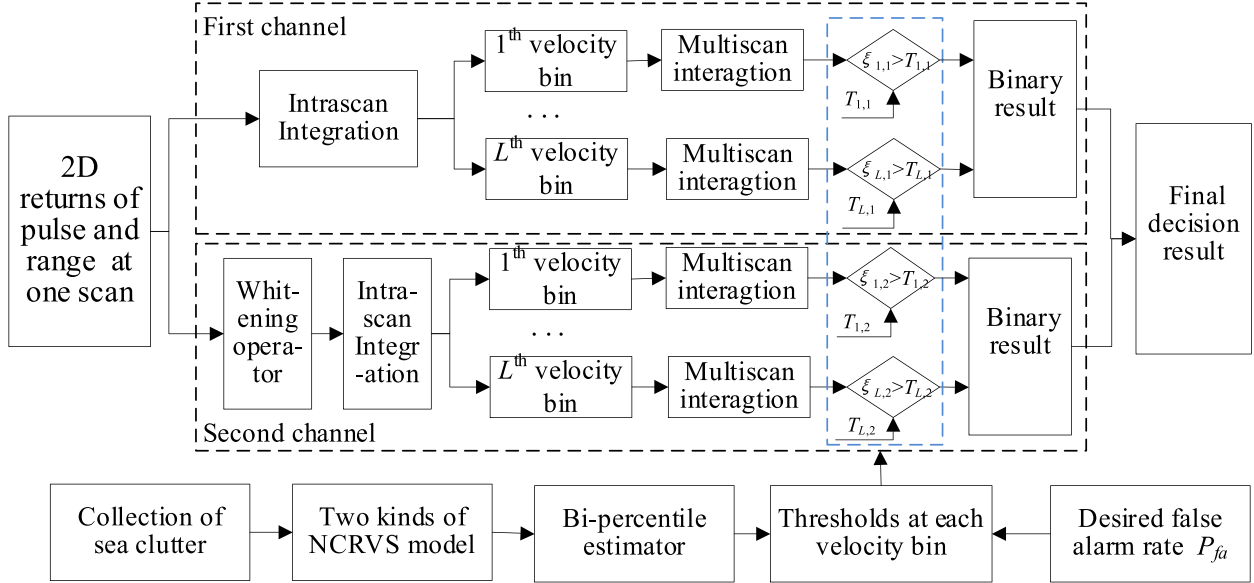
Fig. 9. Flow diagram of DC-MJD detector.

extra improvement of SCR, laying the fundament for potential performance improvement of marine radars at fast-scan mode. When the Doppler offsets of targets fall inside the main clutter region, both sea clutter and targets are heavily mitigated, leading to significant reduction of SCR. It means that coherent whitening operator can attain considerable performance improvement in the case that high-velocity targets has the Doppler offsets outside main clutter region and may suffer heavy performance loss in the inverse case. Therefore, two complementary channels are combined to fully exploit the improvements of whitening operator and ensure the good performance in all the cases. The first channel is designed for the low-velocity targets, where both the intrascan processing and interscan processing use the noncoherent integration. The second channel consists of the first channel plus the whitening operator. It is designed for the high-velocity targets, where pulse correlation of sea clutter is eliminated and uniform spectrum provides the improvement of SCR.

Besides, large amounts of sea clutter in the current sea environment are collected for the offline training. Two kinds of NCRVS model are established to learn the cross-scale properties of sea clutter. Then, outlier-robust analytical bipercentile estimator is used to estimate the parameters of lognormal distributions at individual velocity bin. The different shape parameters imply the property of structural textures and are related to the threshold at each velocity bin. In this way, the thresholds for the first channel and the second channel can be obtained from the analytical functions in theory without using the Monte Carlo test.

At the lth velocity bin, the threshold is given by

$$T_l = p_{\mathrm{LN}}^{-1}\left(P_{f0}\Big|\widehat{\lambda}_l, \widehat{\eta}_l\right), l = 1, 2, \ldots, L \tag{17}$$

where $\widehat{\lambda}_l, \widehat{\eta}_l$ are the estimated parameters of lognormal distribution and P_{f0} is false alarm rate at each velocity bin. Under the assumption that NCRVS at each velocity is independent, the P_{f0} is determined by

$$P_{f0} = \frac{P_{\mathrm{fa}}}{2 \times L} \tag{18}$$

where P_{fa} is the desired false alarm rate. In fact, NCRVS has correlation at different velocity bin due to the fan-shaped retrospective filters with overlapped regions. It means that the false alarm rate for velocity bins is strictly smaller than the desired false alarm rate.

Fig. 10 plots the thresholds at each velocity bin for the two kinds of NCRVS. It has found that the thresholds in the main clutter RFs are much higher than that in the noise RFs. It is hard for sea clutter at main clutter RFs to cross the high threshold, meaning that sea clutter of structural textures is heavily suppressed. Besides, the thresholds in the first channel are larger than that in the second channel. It is because that whitening operator in the second channel can mitigate sea clutter in a time scale of order of milliseconds. Besides, when the clutter environments change, marine radar should restart the mode to collect large amounts of sea clutter for train and the thresholds for the two kinds of NCRVS should be updated. In this way, the thresholds can adapt to the dynamic clutter environments to guarantee the CFRA property of the DC-MJD detector.

IV. EXPERIMENTAL RESULTS AND EVALUATION

In this section, we evaluate the performance of the DC-MJD detector using real datasets from an open and recognized CSIR database [31]. The experimental radar is operated at the dwelling mode, with a carrier frequency of 9 GHz, range resolution of 15 m, and PRF f_r of 2.5 kHz. The instant wind is 7.71 m/s, wind
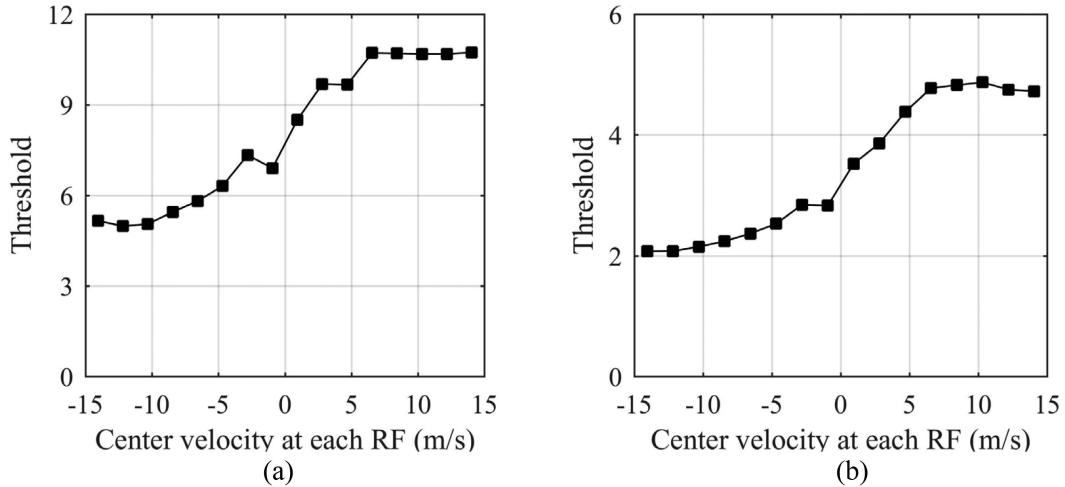
Fig. 10.   Thresholds matching lognormal distributions at two channels. (a) Thresholds in the first channel. (b) Thresholds in the second channel.
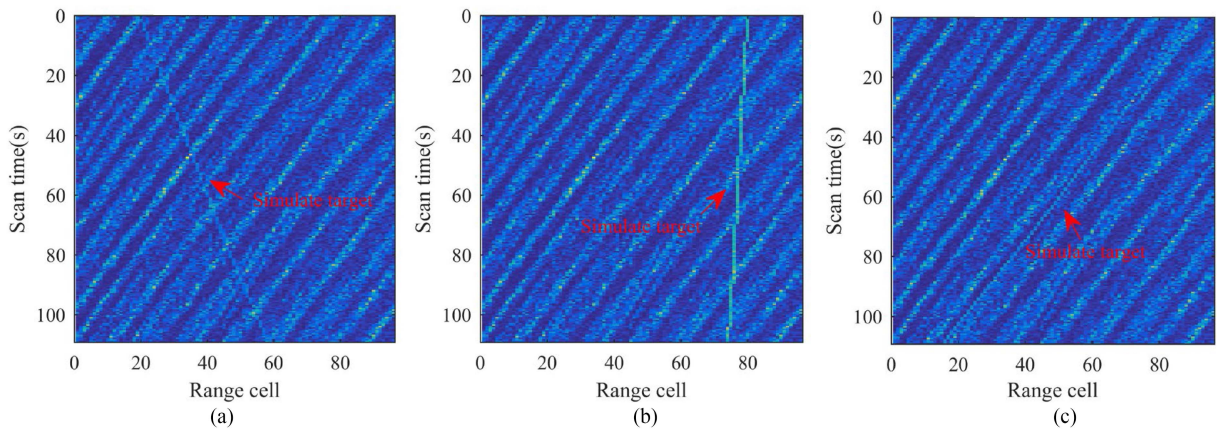

Fig. 11.   Radar returns with simulated targets of different radial velocities. (a) $v = -5$ m/s. (b) $v = 1$ m/s. (c) $v = 10$ m/s.

gust is 11.65 m/s, and significant wave height is 3.24 m. Each dataset consists of 96 range cells and the observation time lasts to 100 s.

A. Real Sea Clutter Data With Simulated Targets

Real dataset (TFC15_002) with pure sea clutter is used to testify the performance of the proposed detector. The dwelling data of pure clutter is downsampled with a period of 0.5 s and pulse number of 8, as shown in Fig. 2. To fully compare performance, simulated targets with different SCRs and radial velocities are linearly added into the scan data. Considering the low velocity of small targets on the sea surface, simulated moving targets follow a weak maneuverable model [31]. At the kth scan, the distance from the target to radar $r(k)$ and the velocity of target $v(k)$ is determined by the parameters in the $(k-1)$th scan. They can be computed by

$$\begin{bmatrix} r(k) \\ v(k) \end{bmatrix} = \begin{bmatrix} 1 & \Delta T \\ 0 & 1 \end{bmatrix} \begin{bmatrix} r(k-1) \\ v(k-1) \end{bmatrix}$$

$$+ \begin{bmatrix} r(k-1) \\ v(k-1) \end{bmatrix} w(k-1) \qquad (19)$$

where w is Gaussian noise sequence. Then, returns of target at mth range is added into real sea clutter and it is given by

$$z(k, m, n) = s(k, m, n) + c(k, m, n)$$
$$= \sqrt{10^{SCR/10}} \rho(k) \exp\left(j \frac{(n-1) 4\pi v(k)}{\lambda_{radar} f_r}\right) \delta$$
$$\times \left(m - \left[\frac{r(k)}{\Delta r}\right]\right)$$
$$+ c(k, m, n), n = 1, 2, \ldots, N \qquad (20)$$

where $\delta(.)$ is impulse function, $\rho(k)$ is unite-mean random sequence that is related to amplitude fluctuation of target, and λ_{radar} is the wave length of radar carrier frequency.

Fig. 11 plots the radar returns with simulated targets of different radial velocities of -5, 1, and 10 m/s and different SCRs of 2, 10, and 5 dB. It represents three typical cases. In Fig. 11(a), the first case is that the Doppler offsets of targets fall
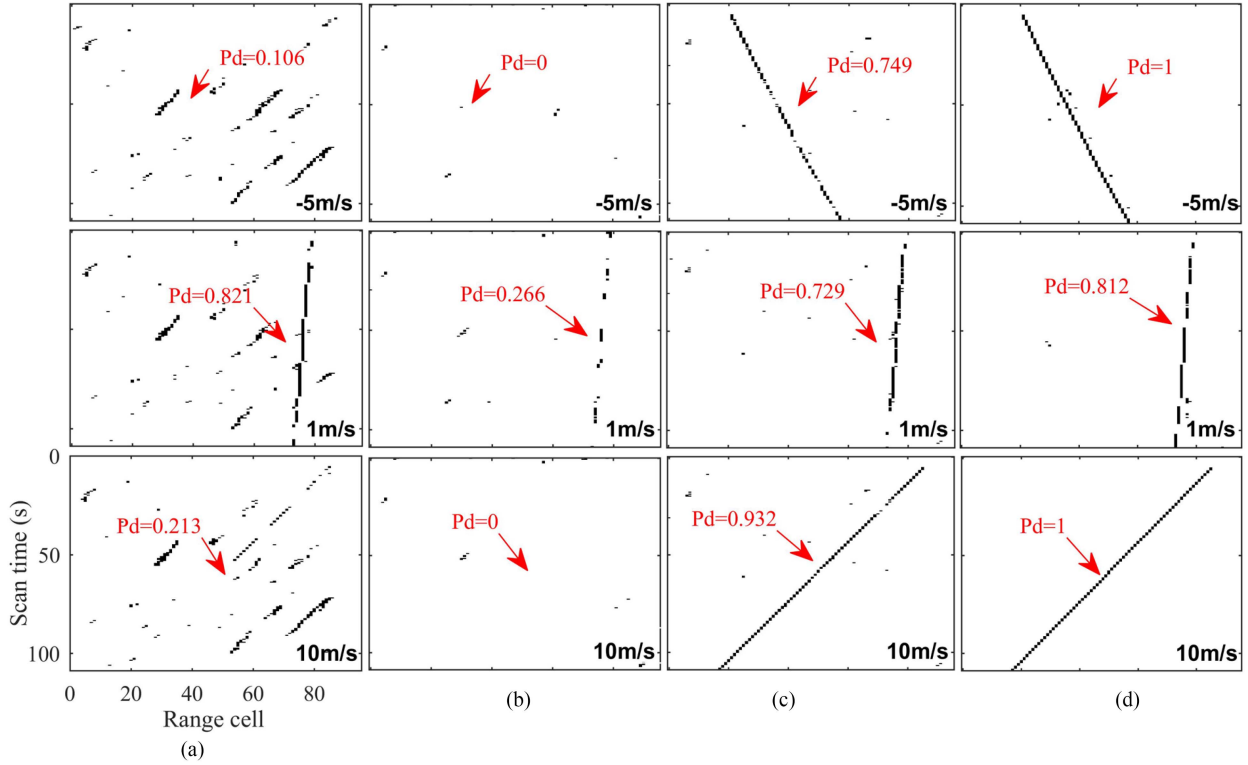
Fig. 12. Performance comparison of four detectors in the dataset with simulated target ($N = 8$, $K = 12$, $P_{fa} = 10^{-3}$). (a) RFB-LogCFAR [15]. (b) FSSIP [18]. (c) DGRF-GLRT-LTD [19]. (d) DC-MJD.
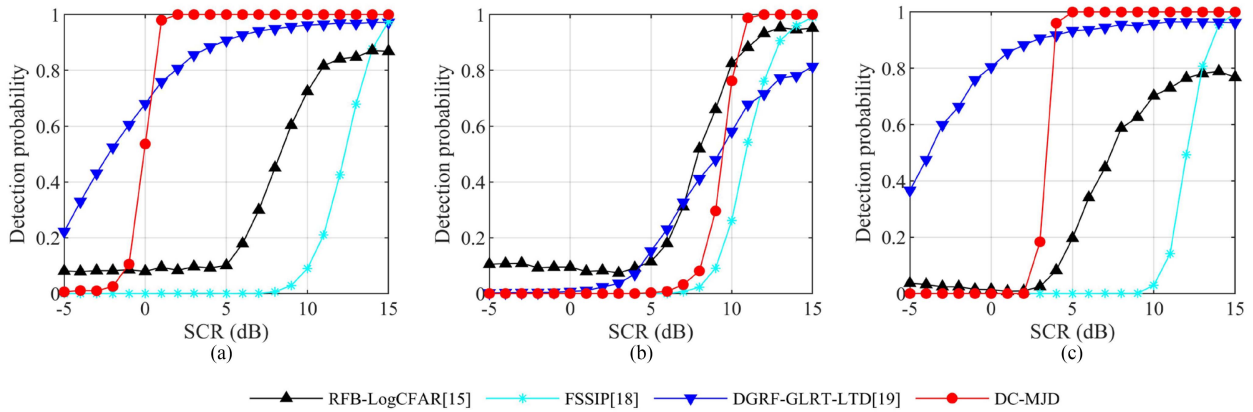

Fig. 13. Performance comparison at different SCRs ($N = 8$, $K = 12$, $P_{fa} = 10^{-3}$). (a) v $= -5$m/s. (b) v $= -1$m/s. (c) v $= -10$m/s.

outside main clutter region in frequency domain and its moving trajectory is totally inconsistent with the moving trajectories of swells and large-scale waves. In Fig. 11(b), the second case is that Doppler offsets of targets fall inside main clutter region and its trajectory is slightly inconsistent with the moving trajectories of structural textures. In Fig. 11(c), the third case is Doppler offsets of targets outside the main clutter region and the moving trajectories of targets submerged in the structural textures during the observation time. To sum up, the high-velocity targets are in the first and the second cases and the low-velocity targets in the second case.

In the first experiments, set $N = 8$, $K = 12$, $P_{\text{fa}} = 10^{-3}$. In Fig. 12(a), RFB-LogCFAR detector [15] can hardly control false alarm rate, due to numerous falsely targets along the bright stripes. Especially at the second case, its detection probability is 0.821 with more false alarm range cells compared to the given $P_{\text{fa}} = 10^{-3}$. In Fig. 12(b), FSSIP detector [18] can control the false alarm rate at the cost of significant performance loss, where noncoherent detector can hardly work. Obviously, mitigating integration along structural textures is absent in the design of FSSIP detector. In Fig. 12(c), DGRF–GLRT–LTD detector [19] has great performance improvement relative to the previous two
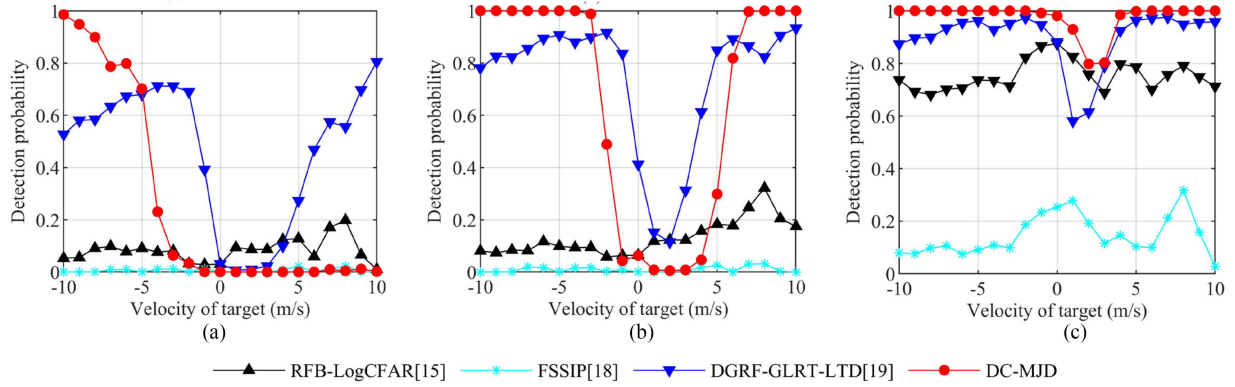
Fig. 14.   Performance comparison at different radial velocities of targets ($N = 8$, $K = 12$, $P_{fa} = 10^{-3}$). (a) SCR = 0 dB. (b) SCR = 5 dB. (c) SCR = 10 dB.
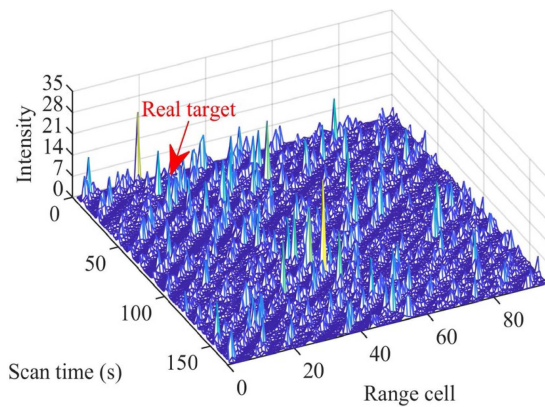

Fig. 15.   Intensity of real dataset in scan-range 2-D grids.

noncoherent detectors, which uses Doppler guidance to avoid the integration along structural textures. Its performance heavily depends on the accuracy estimation of target's Doppler offset, meaning that enough pulses are required for coherent detector. In Fig. 12(d), proposed DC-MJD detector improves the detection probability by 33.5%, 11.4%, and 7.3%, respectively, in the three cases, compared with the DGRF–GLRT–LTD detector [19]. It is clearly found that the simulated moving targets have distinct and continuous moving trajectories in the all three cases. The main advantage of the proposed detector is the mitigation clutter matching the lognormal-distributed NCRVS with different threshold at each velocity bin, particularly heavy suppression in main clutter RFs. In addition, two channels can complement each other to attain robust performance in the different cases.

Besides, we analyze the influence of SCR and target's radial velocity on the detection performance for the four detectors in Figs. 13 and 14. For the RFB-LogCFAR detector [15] and FSSIP detector [18], they suffer from great performance loss in the low SCR case, especially the former mistakes the range cells along the structural textures of sea clutter as targets with the constant detection probabilities of 0.1 when the SCRs are lower than 5 dB. With the complete noncoherent integrations in detection, their good detection performance highly depends on the high SCRs. Simultaneously, the noncoherent integration can ensure

the independence of their performance on the target's velocities, as shown in Fig. 14. Therefore, above two noncoherent detectors are solely suitable for the homogeneous clutter environments with high SCRs, due to the failure to mitigate the integration along the structural textures.

Differently, DGRF–GLRT–LTD detector [19] and the proposed DC-MJD detector can attain good performance, where the former exploits the Doppler guides to avoid the integration along the structural textures and the latter designs the NCRVS models with different threshold to mitigate the integration from the structural textures. In fact, besides the SCR, their performance is also closely related to target's radial velocity. In other words, the target's radial velocity determines the distance between the Doppler offsets of targets and main clutter region in Doppler domain, which plays great role in the coherent detection. In the first case [Fig. 13(a)] and the second case [Fig. 13(c)], DGRF–GLRT–LTD detector [19] can still work when the SCR is lower than 0 dB, owing to the coherent optimal GLRT–LTD detection in the intrascan processing. However, in the second case [Fig. 13(b)], the intrascan GLRT–LTD can hardly work when the Doppler offsets of targets fall inside the main clutter region. It means that the DGRF–GLRT–LTD detector [19] is suitable for the low SCR and the Doppler offsets of targets outside the main clutter region at the same time. As the SCR reaches 5 dB, the proposed DC-MJD detector can attain better performance than DGRF–GLRT–LTD detector [19], as shown in Fig. 13. Thus, it is often required enough SCR to make the noncoherent intrascan integration after whitening operator attain comparable performance as the optimal GLRT–LTD. However, it has found in Fig. 14(b) that both DGRF–GLRT–LTD detector [19] and proposed detector still suffers from great loss when the velocities of targets are around 2 m/s. It implies that the SCR of 5 dB is not enough to eliminate the influence of the Doppler offsets of targets inside main clutter region and it needs the SCR up to 10 dB. In Fig. 14(c), it is clearly shown that the proposed detector achieves the best performance at different velocities of targets, compared with the other three existing detectors, thanks to the mitigation of sea clutter in the intrascan processing and the interscan processing. In terms of the enough high SCR, the target's velocity is no longer the main factor to affect the detection performance. Instead, good performance mainly lies
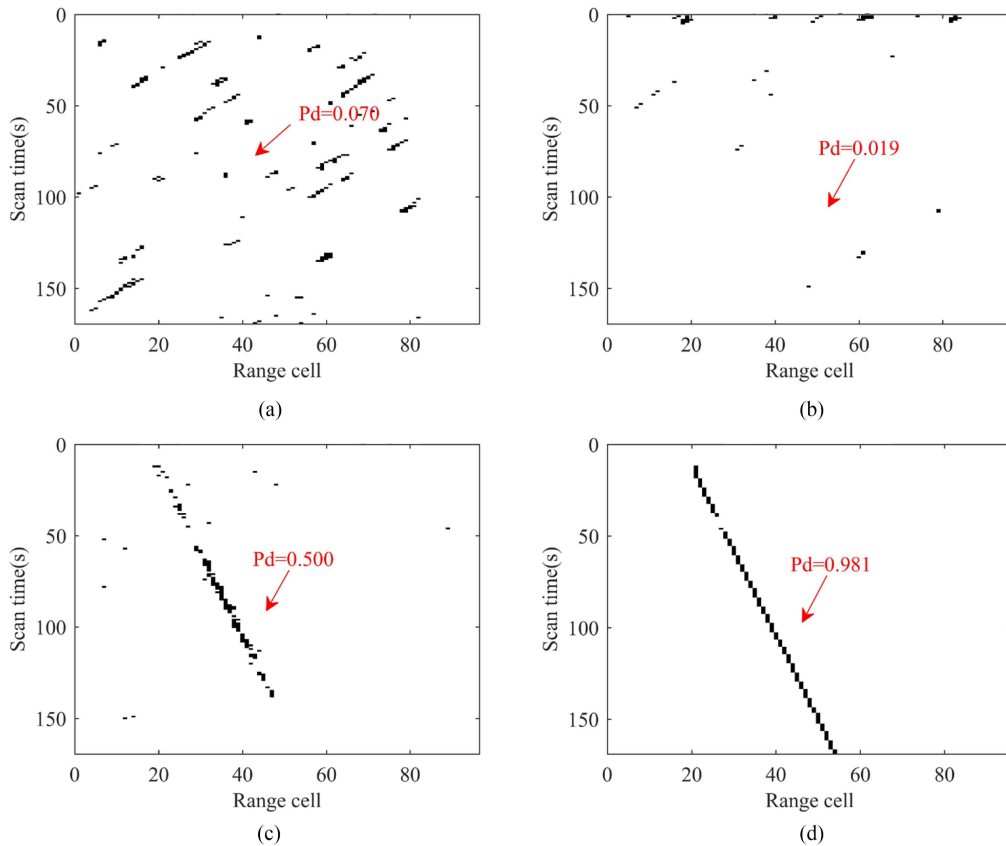
Fig. 16. Performance comparison in real dataset with real target ($N = 8$, $K = 12$, $P_{fa} = 10^{-3}$). (a) RFB-LogCFAR [15]. (b) FSSIP [18]. (c) DGRF–GLRT–LTD [19]. (d) DC-MJD.

in the mitigation of the integration along structural textures in the time scale of the order of seconds. This is the main invocation of the lognormal-distributed NCRVS model in this article. To sum up, DGRF–GLRT–LTD detector [19] is suggested for the low SCR case of Doppler offsets of targets outside main clutter region. For the SCRs higher than 5 dB, the proposed DC-MJD detector can ensure it appropriate for real complicated clutter environments.

B. Real Data With Test Target

Below, real dataset (TFC15_008) with test target is further used to evaluate the performance of the four detectors in the sea clutter with structural textures. Similarly, the dwelling data is transformed to the scan data with a period of 1 s and the pulse number of eight. The test target is a wave rider rigid inflatable boat of 5.7 m in length. Fig. 15 gives the intensity of scan data in the scan-range time 2-D plane. Though the average SCR is roughly estimated of 6.8 dB, the returns of targets fluctuate sharply in a large region, where the returns of targets are completely submerged in sea clutter during the scan time from 150 to 169 s.

In the second experiments, we remain the same settings as the first experiments. In Fig. 16(a) and (b), both RFB-LogCFAR detector [15] and FSSIP detector [18] fail to work, suffering great performance loss when sea clutter exhibits structural textures.

In Fig. 16(c) and (d), relative to DGRF–GLRT–LTD detector [19], DC-MJD detector has the detection probability of 0.981, improving performance by 96.2%. In this case, the first channel plays the main role in the proposed DC-MJD detector, since the Doppler offsets of targets fall outside the main clutter region and the moving trajectories are inconsistent with the radial velocity of swells and large-scale waves. Thus, the whitening operator and lognormal-distributed NCRVS with the different thresholds can mitigate the sea clutter in the intrascan processing and the interscan processing in this case. Besides, the proposed DC-MJD detector can provide a rough estimation of target's radial speed as -3 m/s and swell's radial speed as 9 m/s, according to test statistics over threshold from the seventh RF and the main clutter RFs. While the DGRF—GLRT–LTD detector [11] can only provide target's radial velocity using enough coherent pulses at one scan.

In the real radar system, small target detection needs observation time of several seconds. The selection of suitable detector is generally according to the practical requirements. When the number of pulses is enough at one scan, DGRF–GLRT–LTD [19] is suggested for coherent radar. When the number of pulses is less than 10, DC-MJD detector is the first choice. In addition, DGRF–GLRT–LTD [19] is specified for the case that the Doppler offsets of targets fall outside the main sea clutter bins in the low SCR case. Differently, DC-MJD detector can attain good performance in all the cases with the

SCR higher than 5 dB, thanks to the lognormal-distributed NCRVS model and the structure of two complementary channels.

V. Conclusion

This article deals with the problem of small target detection in the spatial–temporally sea clutter with structural textures. We extract the swell's movement property using a new NCRVS model of sea clutter in across time scales from the order of milliseconds to the order of seconds. The NCRVS can be well-fitted by the lognormal distribution at each velocity bin, where an outlier-robust analytical bipercentile estimator is presented to estimate the unknown parameters of the lognormal distribution. Based on the lognormal-NCRVS model, a DC-MJD detector is proposed with whitened operator and different thresholds at each velocity bin to successfully suppress sea clutter. The proposed DC-MJD detector can attain good performance in the complicated clutter environments, showing that it is indeed an effective way to improve the detection of sea-surface small targets by exploiting the new-span property of sea clutter with structural textures. In the future article, it can further elaborate statistical properties of spatial–temporally sea clutter, such as correlation of NCRVS at each velocity bin, in order to improve detection performance of small targets when high-resolution marine radar is operated at fast-scan mode.

References

[1] Y. Yang, S. P. Xiao, and X.-S. Wang, "Radar detection of small target in sea clutter using orthogonal projection," *IEEE Geosci. Remote Sens. Lett.*, vol. 16, no. 3, pp. 382–386, Mar. 2019.

[2] X. Liang, P. L. Shui, and H. T. Su, "Bi-phase compound-Gaussian mixture model of sea clutter and scene-segmentation-based target detection," *IEEE J. Sel. Topics Appl. Earth Observ. Remote Sens.*, vol. 14, pp. 4661–4674, Apr. 2021.

[3] K. Yan, Y. Bai, H. Wu, and X. Zhang, "Robust target detection within sea clutter based on graphs," *IEEE Trans. Geosci. Remote Sens.*, vol. 57, no. 9, pp. 7093–7103, Sep. 2019.

[4] T. Li, D. Peng, and S. Shi, "Outlier-robust superpixel-level CFAR detector with truncated clutter for single look complex SAR images," *IEEE J. Sel. Topics Appl. Earth Observ. Remote Sens.*, vol. 15, pp. 5261–5274, Jun. 2022.

[5] K. Yan, Y. Bai, H. Wu, and X. Zhang, "Robust target detection within sea clutter based on graphs," *IEEE Trans. Geosci. Remote Sens.*, vol. 57, no. 9, pp. 7093–7103, Sep. 2019.

[6] K. D. Ward, R. J. A. Tough, and S. Watts, *Sea Clutter Scattering: The K Distribution and Radar Performance*. London, U.K.: The Institution of Engineering and Technology, 2013.

[7] C. M. Javier, G. M. Javier, B. C. Alvaro, and A. L. Alberto, "Statistical analysis of a high-resolution sea-clutter database," *IEEE Trans. Geosci. Remote Sens.*, vol. 48, no. 4, pp. 2024–2037, Apr. 2010.

[8] H. Yu et al., "Bipercentile parameter estimators of bias reduction for generalised Pareto Clutter model," *IET Radar, Sonar Navigation*, vol. 14, no. 7, pp. 1105–1112, 2020.

[9] E. Ollila, D. E. Tyler, V. Koivunen, and H. Vincent Poor, "Compound-Gaussian clutter modeling with an inverse Gaussian texture distribution," *IEEE Signal Process. Lett.*, vol. 19, no. 12, pp. 876–879, Dec. 2012.

[10] A. Farina, A. Russo, and A. Studer, "Coherent radar detection in log-normal clutter[J]," *IEE Proc. Part F - Commun., Radar Signal Process.*, vol. 133, no. 1, pp. 39–53, 1986.

[11] J. Xue, S. Xu, J. Liu, and P. Shui, "Model for non-Gaussian sea clutter amplitudes using generalized inverse Gaussian texture," *IEEE Geosci. Remote Sens. Lett.*, vol. 16, no. 6, pp. 892–896, Jun. 2019.

[12] L. Rosenberg, D. J. Crisp, and N. J. Stacy, "Analysis of the KK-distribution with medium grazing angle sea-clutter," *IET Radar Sonar Navigation*, vol. 4, no. 2, pp. 209–222, 2010.

[13] M. Greco, F. Bordoni, and F. Gini, "X-band sea-clutter nonstationarity: Influence of long waves," *IEEE J. Ocean. Eng.*, vol. 29, no. 2, pp. 269–283, Apr. 2004.

[14] H. Ding, J. Guan, N. Liu, and G. Wang, "New spatial correlation models for sea clutter," *IEEE Geosci. Remote Sens. Lett.*, vol. 12, no. 9, pp. 1833–1837, Sep. 2015.

[15] J. G. Shannon and P. M. Moser, "A history of US Navy periscope detection radar sensor design and development," *U. S. Navy J. Underwater Acoust.*, vol. 61, no. 2, pp. 203–231, 2014.

[16] J. J. Ousborne, D. Griffith, and R. W. Yuan, "A periscope detection radar," *Johns Hopkins APL Tech. Dig.*, vol. 19, no. 1, pp. 125–133, 1997.

[17] M. McDonald and S. Lycett, "Fast versus slow scan radar operation for coherent small target detection in sea clutter," *IEE Proc. Radar, Sonar Navigation*, vol. 152, no. 6, pp. 429–435, 2005.

[18] S. D. Blunt, K. Gerlach, and J. Heyer, "HRR detector for slow-moving targets in sea clutter," *IEEE Trans. Aerosp. Electron. Syst.*, vol. 43, no. 3, pp. 965–974, Jul. 2007.

[19] B. Jin, Y. Ma, and G. Wu, "Fast scan-to-scan integration algorithm for small target in sea clutter," *Electron. Lett.*, vol. 53, no. 15, pp. 1070–1071, 2017.

[20] S. N. Shi, X. Liang, P. L. Shui, and S. Zhang, "Low-velocity small target detection with Doppler-guided retrospective filter in high-resolution radar at fast scan mode," *IEEE Trans. Geosci. Remote Sens.*, vol. 57, no. 11, pp. 8937–8953, Nov. 2019.

[21] S. Watts, K. D. Ward, and R. J. A. Tough, "The physics and modelling of discrete spikes in radar sea clutter," in *Proc. IEEE Int. Radar Conf.*, 2005, pp. 72–77.

[22] N. Valeyrie, R. Garello, J. Quellec, and M. Chabah, "Study of the modeling of radar sea clutter using the KA distribution and methods for estimating its parameters," in *Proc. Int. Radar Conf. "Surveillance for a Safer World"*, 2009, pp. 1–6.

[23] M. Greco, P. Stinco, and F. Gini, "Identification and analysis of sea radar clutter spikes," *IET Radar Sonar Navigation*, vol. 4, no. 2, pp. 239–250, Apr. 2010.

[24] E. Bahar and R. D. Kubik, "Tilt modulation of high resolution radar backscatter cross sections: Unified full wave approach," *IEEE Trans. Geosci. Remote Sens.*, vol. 31, no. 6, pp. 1229–1242, Nov. 1993.

[25] M. Weiss, "Analysis of some modified cell-averaging CFAR processors in multiple-target situations," *IEEE Trans. Aerosp. Electron. Syst.*, vol. 18, no. 1, pp. 102–114, Jan. 1982.

[26] W. Zhou, J. Xie, G. Li, and Y. Du, "Robust CFAR detector with weighted amplitude iteration in nonhomogeneous sea clutter," *IEEE Trans. Aerosp. Electron. Syst.*, vol. 53, no. 3, pp. 1520–1535, Jun. 2017.

[27] F. Gini and M. Greco, "Covariance matrix estimation for CFAR detection in correlated heavy tailed clutter," *Signal Process.*, vol. 82, no. 12, pp. 1847–1859, 2002.

[28] H. Sittrop, "On the sea-clutter dependency on wind speed," in *Proc. IEE Radar Conf.*, 1977, pp. 110–114.

[29] J. P. Reilly and G. D. Dockery, "Influence of evaporation ducts on radar sea return," *IEE Proc. F-Radar Signal Process.*, vol. 137, no. 2, pp. 80–88, 2002.

[30] A. P. Trujillo and H. V. Thurman, *Essentials of Oceanography*, 11th ed. Saddle River, NJ, USA: Pearson Education, 2014.

[31] T. Lamont-Smith, "Azimuth dependence of Doppler spectra of sea clutter at low grazing angle," *IET Radar, Sonar Navigation*, vol. 2, no. 2, pp. 97–103, Apr. 2008.

[32] Accessed: Oct. 11, 2012. [Online]. Available: http://www.csir.co.ca/small_boat_detection

[33] M. Chittapur and K. Sharavana, "Track-before-detection technique for mitigating sea clutter based on Hough transform," *Int. J. Comput. Sci. Netw.*, vol. 3, no. 3, pp. 66–70, 2014.

[34] X. Rong Li and V. P. Jilkov, "Survey of manoeuvring target tracking. Part I. Dynamic models," *IEEE Trans. Aerosp. Electron. Syst.*, vol. 39, no. 4, pp. 1333–1364, Oct. 2003.

[35] M. I. Skolnik, *Introduction to Radar Systems*, 3rd ed. New York, NY, USA: McGraw-Hill, 2001, Ch. 3, p. 142.

[36] Z. Bao, X. Peng, and S. Zhang, "Study of weather clutter rejection with moving target detection (MTD) processor," in *Proc. Int. Conf. Radar*, 1982, pp. 56–60.

[37] S. Xu, J. Zhu, J. Jiang, and P. Shui, "Sea-surface floating small target detection by multifeature detector based on isolation forest," *IEEE J. Sel. Topics Appl. Earth Observ. Remote Sens.*, vol. 14, pp. 704–715, Oct. 2021.

[38] H. Zhou and T. Jiang, "Decision tree based sea-surface weak target detection with false alarm rate controllable," *IEEE Signal Process. Lett.*, vol. 26, no. 6, pp. 793–797, Jun. 2019.

[39] F. T. Gu, "Detection of small floating targets on the sea surface based on multi-features and principal component analysis," *IEEE Geosci. Remote Sens. Lett.*, vol. 17, no. 5, pp. 809–813, May 2020.

[40] P. Shui, D. Li, and S. Xu, "Tri-feature-based detection of floating small targets in sea clutter," *IEEE Trans. Aerosp. Electron. Syst.*, vol. 50, no. 2, pp. 1416–1430, Apr. 2014.

[41] K. J. Sangston, F. Gini, and M. S. Greco, "Coherent radar target detection in heavy-tailed compound-Gaussian clutter," *IEEE Trans. Aerosp. Electron. Syst.*, vol. 48, no. 1, pp. 64–77, Jan. 2012.

Xiang Liang was born in 1994. He received the B.S. degree in electrical engineering, in 2017, from the Xidian University, Xi'an, China, where he is currently working toward the Ph.D. degree in signal and information processing with the National Laboratory of Radar Signal Processing.

His research interests include radar signal simulation and weak target detection in sea clutter.

Sai-Nan Shi was born in 1990. She received the B.S. degree in electrical engineering and the Ph.D. degree in information and signal processing from the Xidian University, Xi'an, China, in 2013 and 2018, respectively.

She is currently an Associate Professor with the School of Electronic and Information Engineering, Nanjing University of Information Science and Technology, Nanjing, China. Her research interests include radar signal processing and weak target detection in sea clutter.

Tao Li was born in 1992. She received the B.S. degree in electrical engineering and the Ph.D. degree in pattern recognition and intelligent system from the Xidian University, Xi'an, China, in 2013 and 2019, respectively.

She is currently a Lecturer with the School of Automation, Hangzhou Dianzi University, Hangzhou, China. Her research interests include SAR image processing, target detection, and recognition.

Peng-Lang Shui (Senior Member, IEEE) was born in 1967. He received the M.S. degree in mathematics from the Nanjing University, Nanjing, China, in 1992, and the Ph.D. degree in electrical engineering from the Xidian University, Xi'an, China, in 1999.

He is currently a Professor with the National Laboratory of Radar Signal Processing, Xidian University. His research interests include sea clutter modeling and analysis, radar target detection, and image processing.